Site-selective correlations in interacting flat-band quasicrystals

Yuxi Zhang [1,2] Richard T. Scalettar [3] and Rafael M. Fernandes [1,2]

[1]*Department of Physics, The Grainger College of Engineering, University of Illinois Urbana-Champaign, Urbana, Illinois 61801, USA*

[2]*Anthony J. Leggett Institute for Condensed Matter Theory, The Grainger College of Engineering, University of Illinois Urbana-Champaign, Urbana, Illinois 61801, USA*

[3]*Department of Physics, University of California, Davis, California, USA*

(Received 21 October 2024; revised 4 April 2025; accepted 7 July 2025; published 24 July 2025)

Model lattices such as the kagome and Lieb lattices have been widely investigated to elucidate the properties of interacting flat-band systems. While a quasicrystal does not have proper bands, the noninteracting density of states of several of them displays the typical signature of a flat band pinned at the Fermi level: a delta-function zero-energy peak. Here, we employ quantum Monte Carlo simulations to determine the effect of onsite repulsion on these quasicrystals. While global properties such as the antiferromagnetic structure factor and the specific heat behave similarly as in the case of periodic lattices undergoing a Mott transition, the behavior of the local density of states depends on the coordination number of the site. In particular, sites with the smallest coordination number, which give the dominant spectral-weight contribution to the zero-energy peak, are the ones most strongly impacted by the interaction. Besides establishing site-selective correlations in quasicrystals, our work also points to the importance of the real-space structure of flat bands in interacting systems.

DOI: 10.1103/77l3-krmj

I. INTRODUCTION

Flat-band systems provide a unique framework to expand our conceptual understanding of strongly-correlated electronic systems. Because of the vanishingly small bandwidth, the electron-electron interaction has a strong impact on the electronic spectrum, even if it is small in absolute value. For this reason, flat bands have been theoretically and experimentally investigated in diverse settings [1,2], from moiré systems tuned to special twist-angle values [3–5] to geometrically-frustrated lattices such as kagome [6–9] and pyrochlore [10].

A system that has been less explored in this context are quasiperiodic crystals [11,12]. Since proper bands cannot be defined, the electronic spectrum of quasicrystals is assessed via the density of states (DOS). In a periodic lattice, a flat band is manifested as a delta-function peak in the DOS, since the integrated DOS is discontinuous. Interestingly, in several quasicrystals, including the Penrose tilings known as kite-and-dart (or P2) and rhombus (or P3), a delta-function peak pinned at zero energy is found in the DOS [13–15]. These peaks are the manifestation of a macroscopic number of zero-energy states, corresponding to approximately 10% of all states in the Penrose tiling. Despite the similarities between the zero-energy peaks of the P2 and P3 tiling, their microscopic origins and real-space distributions are quite different [16].

Theoretical interest in interacting quasicrystals has surged in recent years [17–39], partly motivated by the experimental observation of correlated phenomena such as superconductivity [40–42], magnetism [43–45], and quantum criticality [46–48]. Moreover, quasicrystalline patterns have been engineered in diverse settings such as optical lattices [49–51], photonic lattices [52,53], moiré superlattices [41,42,54], and synthetic lattices [55] thus significantly expanding the opportunities to tune, probe, and control quasicrystals. Despite such an intense activity, a systematic investigation of the role of flat bands in interacting quasicrystals remains little explored.

In this paper, we elucidate the fate of flat-band quasicrystals in the presence of strong electron-electron interactions. In particular, we use the exact and unbiased determinantal quantum Monte Carlo (DQMC) method [56–58] to solve the Hubbard model on both the rhombus and the kite-and-dart Penrose tiling. We find that global quantities such as the specific heat and the antiferromagnetic structure factor display similar signatures of a Mott transition as those observed in periodic lattices [59,60], indicative of a Mott transition at $U^*/t \approx 3.5$ (see also Refs. [18,21]). Here, U is the onsite Hubbard interaction and t is the nearest-neighbor hopping parameter.

Motivated by the fact that these quasicrystals have sites with different coordination numbers $3 \leqslant z \leqslant 7$, we also probe local properties by computing a proxy for the zero-energy local density of states (LDOS), i.e., a quantity available in DQMC that does not require analytical continuation and that is related to the actual LDOS. Previous real-space dynamical mean-field theory (DMFT) calculations of the Hubbard model on a Penrose quasicrystal identified site-dependent double occupancy and renormalization factors whose origin remains unsettled [18]. Our main result is the observation of site-selective correlations in the strong-coupling regime of $U > U^*$. While at high temperatures the LDOS proxy is the largest at the sites with the smallest coordination z, this trend reverses below a characteristic temperature T^*, where the sites with the smallest z value display the smallest LDOS proxy values. Interestingly, T^* extrapolates to zero close to the characteristic interaction strength U^* where the global Mott transition is estimated. By analyzing the frequency-dependent LDOS at each site via analytical continuation, we confirm that different sites are impacted in distinct ways by interactions, with larger

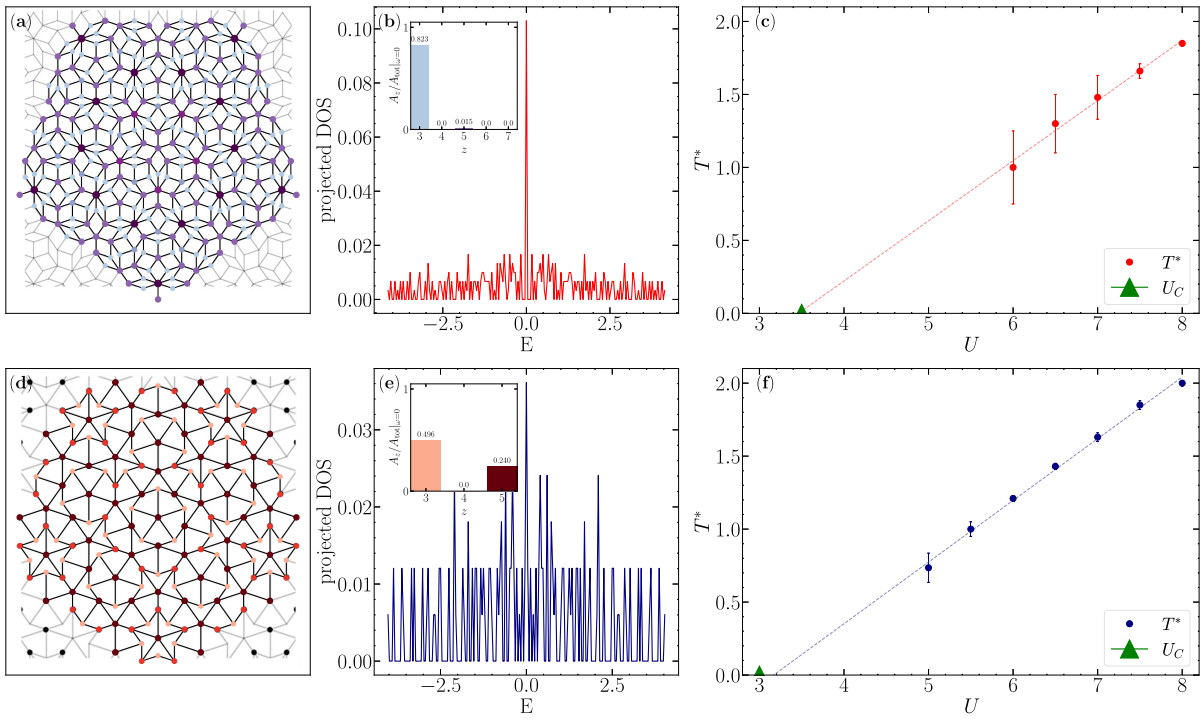

FIG. 1. (a) Penrose rhombus tiling; sites are colored according to their coordination number $3 \leqslant z \leqslant 7$. (b) Density of states for the $N = 301$ tiling studied here. (Inset) Zero-energy spectral-weight ratio $A_z/A_{\rm tot}|_{\omega=0}$, highlighting the dominant contribution from the $z = 3$ sites. (c) Crossing temperature T^* of the DOS proxy curves, shown in Fig. 3, as a function of U. The dashed line is a linear interpolation. Only nonzero T^* values (red circles) that could be unambiguously resolved are shown. U_c (green triangle) is the critical U value extracted from the specific heat analysis. [(d)–(f)] Same as (a)–(c), but for the Penrose kite-and-dart tiling, where $3 \leqslant z \leqslant 5$ and $N = 166$. In all figures of this paper, we set $t = 1$.

gaps emerging for sites with smaller z. Interestingly, the sites that are the most strongly impacted by correlations are also those that contribute the most spectral weight to the noninteracting zero-energy peak of the global DOS, revealing a subtle interplay between interactions and flat bands.

This paper is structured as following: In Sec. II, we will introduce the model and method used in this study. Results from rhombus tiling and kite-and-dart tiling will be introduced in Secs. III A and III B, respectively. Finally a discussion and summary will be presented in Sec. IV.

II. MODEL AND METHODOLOGY

Our starting point is the half-filled Hubbard model [61,62]:

$$\hat{\mathcal{H}} = -\sum_{\langle \mathbf{i},\mathbf{j}\rangle,\sigma} (t\, \hat{c}^{\dagger}_{\mathbf{i}\sigma}\hat{c}_{\mathbf{j}\sigma} + \text{H.c.}) + U\sum_{\mathbf{i}} \left(\hat{n}_{\mathbf{i},\uparrow} - \frac{1}{2}\right)\left(\hat{n}_{\mathbf{i},\downarrow} - \frac{1}{2}\right), \quad (1)$$

where $\hat{c}_{\mathbf{i}}$ is the annihilation operator for an electron on site $\mathbf{i}$ and spin σ, and $\hat{n}_{\mathbf{i}} = \hat{c}^{\dagger}_{\mathbf{i}}\hat{c}_{\mathbf{i}}$ is the number operator. Hereafter, we set $t = 1$. The two types of Penrose quasicrystals studied here are shown in Figs. 1(a) and 1(d), corresponding to the rhombus and kite-and-dart tiling, respectively, both of which are bipartite. In the figure, the sites are colored according to their coordination number z [see insets of panels (b) and (e)], which assume values in the range $3 \leqslant z \leqslant 7$ for the rhombus tiling and $3 \leqslant z \leqslant 5$ for the kite-and-dart tiling. The sites marked in Figs. 1(a) and 1(d) form the finite-size aperiodic lattices with open boundary conditions used in our DQMC simulations, with $N = 301$ sites (rhombus) and $N = 166$ sites (kite-and-dart), constructed to explicitly preserve the fivefold symmetry of the Penrose geometry. We also considered smaller and larger sizes, and found that our main results are robust for different N values (see Appendix B).

The noninteracting ($U = 0$) electronic spectra of both tilings are characterized by delta-function zero-energy peaks in the DOS in the thermodynamic limit [13,14,16]. Figures 1(b) and 1(e) demonstrate that the DOS of our finite-size tilings display these zero-energy peaks. Noticeably, not all sites contribute equally to the zero-energy peak. When projected onto the coordination number z, the zero-energy DOS is found to be dominated by the sites with $z = 3$ in both geometries, as shown by the z-resolved relative spectral function calculated at zero energy, $A_z/A_{\rm tot}|_{E=0}$ [insets of Figs. 1(b) and 1(e)]. The sum is smaller than 1 because the boundary sites are excluded due to the open boundary conditions used here.

To investigate the impact of U, we solve Eq. (1) via DQMC, an exact and unbiased method that does not have the sign-problem since the model (1) is particle-hole symmetric (additional details, including the parameters used, are introduced in Appendix A). Error bars are presented in all plots

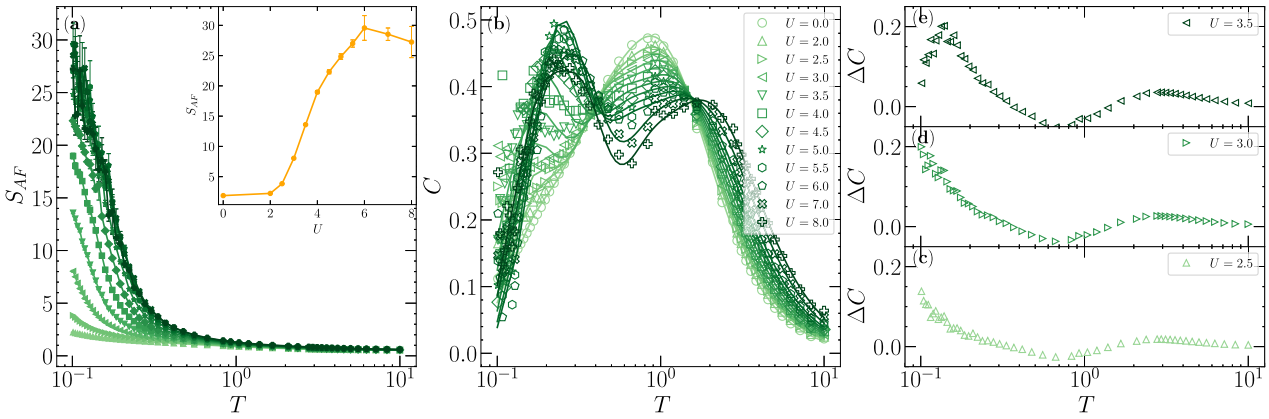

FIG. 2. Antiferromagnetic structure factor S_{AF} (a) and specific heat C (b) as functions of temperature T for the rhombus tiling. The colors indicate different U values, which increase as the color scale change from light to dark; the inset in (a) shows S_{AF} at low temperature $T = 0.1$. [(c)–(e)] Specific heat difference with respect to the noninteracting case, $\Delta C \equiv C(U) - C(U = 0)$. A low-temperature peak emerges at $U_c = 3.5$.

that include Monte Carlo data, and in most cases, they are smaller that the symbol's size.

III. NUMERICAL RESULTS

A. Rhombus tiling

We start by analyzing the quasicrystal's global properties. Figure 2(a) displays the antiferromagnetic (AF) structure factor S_{AF} as a function of temperature T for multiple interaction strength values. While for small U the system shows no sign of AF order down to the lowest temperatures probed, magnetic correlations are strongly enhanced for $U \gtrsim 3.0$ (see inset), indicative of an AF-Mott transition. Such a transition is also observed by RDMFT calculations, albeit at larger U values [18,30]. This transition is further confirmed by analyzing the specific heat C, Fig. 2(b). For $U \leqslant 3.5$, $C(T)$ shows a broad peak around $T \approx 1.0$, similar to the noninteracting system. However, for $U \geqslant 3.5$, $C(T)$ develops a sharper second peak at lower temperatures, as highlighted in Figs. 2(c)–2(e), where $\Delta C \equiv C(U) - C(U = 0)$ is plotted near $U = 3.5$. A second specific-heat peak is also seen in DMFT and DQMC solutions of the Hubbard model in periodic lattices [59,63–65], where it is attributed to AF correlations. Thus we associate $U^* \approx 3.5$ to a putative AF-Mott transition.

The behaviors of S_{AF} and C in the quasicrystal are very similar to what is seen in periodic lattices undergoing a Mott transition [59]. Meanwhile, the distinguishing feature of the quasicrystal is that its sites have multiple coordination numbers z, which contribute unevenly to the zero-energy peak (i.e., the "flat band"). It is thus desirable to probe the z-resolved spectral function $A_z(\omega) = -\mathrm{Im}G_z(\omega)/\pi$, which encodes the LDOS for a site with coordination number z. Here, $G_z(\omega)$ is the local Green's function averaged over nonboundary sites with same z. While obtaining the frequency-dependent function requires analytical continuation, $A_z(\omega = 0)$ can be estimated via the proxy:

$$W_z(T) = \frac{\beta}{\pi} G_z(\tau = \beta/2) = \beta \int \frac{d\omega}{2\pi} \frac{A_z(\omega)}{\cosh(\beta\omega/2)}, \qquad (2)$$

which involves only the imaginary-time Green's function [66–68]. Indeed, as shown in Fig. 3(a) for the noninteracting case ($U = 0$), the LDOS proxy $W_z(T)$ approaches the analytically calculated $A_z(\omega = 0)$ as $T \to 0$. The fact that

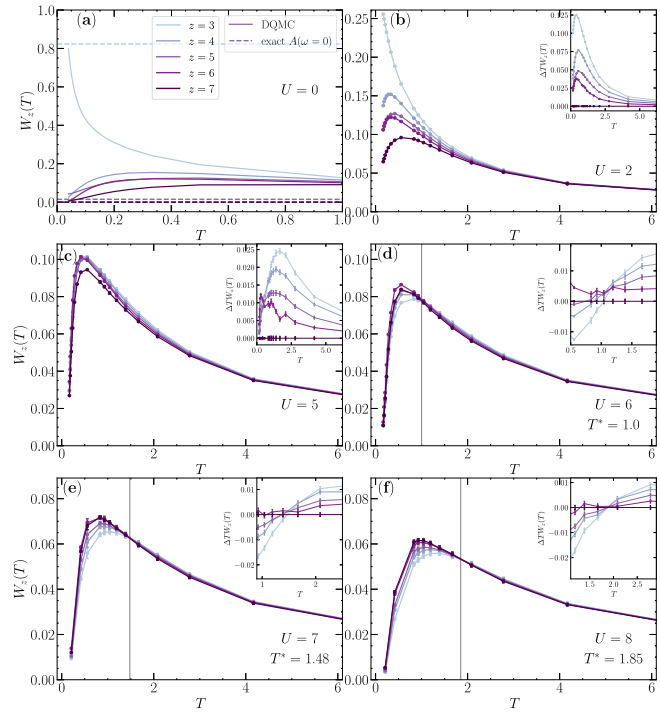

FIG. 3. Proxy $W_z(T)$ for the average local density of states at a site with coordination number z in the rhombus tiling. Each panel shows a different interaction strength U. Different z values are displayed in a light-blue to dark-purple color scale. Both DQMC and analytical results for $A_z(\omega = 0)$ are shown in the noninteracting case in (a). A crossing between the curves is observed in (d)–(f), signaled by a vertical line. The insets in (b)–(f) present $\Delta TW_z(T) \equiv TW_z(T) - TW_7(T)$ to further highlight the presence or absence of crossing points. The range of crossing points between any pair $[TW_z(T), TW_{z'}(T)]$ is used to determine the error bars shown in Fig. 1(c).

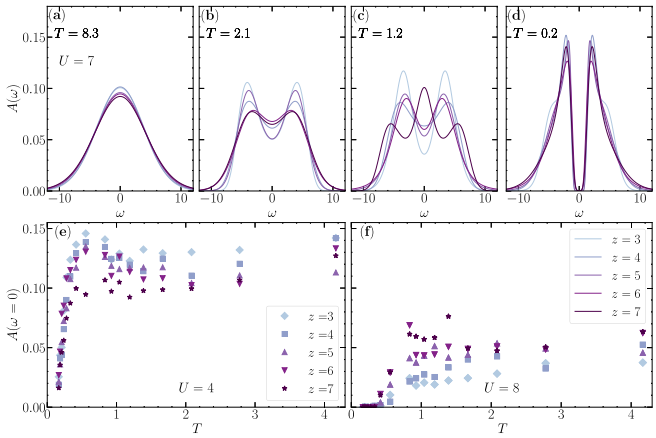

FIG. 4. [(a)–(d)] Evolution of the z-projected spectral function $A_z(\omega)$, obtained via analytical continuation, as temperature T is lowered for fixed $U = 7$ for the rhombus lattice. [(e) and (f)] Zero-energy spectral function $A_z(0)$ as a function of T for $U = 4$ and $U = 8$. In (e), $A_3(0)$ is generally the largest wheres in (f), it is generally the smallest. A gap is clearly seen for all z values in (f).

the proxy only approaches a nonzero value for $z = 3$ and $z = 5$, with $W_3(T \to 0) \gg W_5(T \to 0)$, is a consequence of the zero-energy peak being strongly dominated by the $z = 3$ sites, as shown in Fig. 1(b).

As U increases, two different behaviors emerge in the weak and strong coupling regimes, see Figs. 3(b)–3(f). For $U = 2$ [panel (b)], while all LDOS proxy curves $W_z(T)$ are suppressed with respect to their noninteracting values,$W_3(T)$ remains the largest one as $T \to 0$, i.e., the low-energy DOS remains dominated by the $z = 3$ sites. Meanwhile, for $U = 8$ [panel (f)], the situation is different. Above a characteristic temperature $T^* = 1.85$ (vertical black line), all $W_z(T)$ curves are rather similar, with W_3 slightly larger than the other curves, and W_7 slightly smaller. At T^*, however, the $W_z(T)$ curves cross (highlighted by the inset), and the hierarchy of the LDOS proxy curves is reversed below T^*, with $W_3(T)$ becoming the smallest one. Thus, in the strong-coupling regime, the sites with the smallest coordination numbers are more strongly impacted by the interaction, in that their LDOS proxies are more suppressed than the LDOS proxies of the sites with the largest coordination numbers – despite the fact that the former dominate the low-energy region of the noninteracting spectrum. A similar behavior is observed for $U = 7$ and 6 [panels (e) and (d)], with T^* decreasing for decreasing U, while a clear crossing cannot be resolved for $U = 5$ [panel (c)]. Similar behaviors are observed in the kite-and-dart tiling. In the Appendix, we also show the distribution of W_z for each z value, demonstrating that the behavior of the average value shown in Fig. 3 is representative of the behavior of each site.

It is illuminating to plot the crossing temperatures T^* as a function of U, see Figs. 1(c) (rhombus) and 1(f) (kite-and-dart). A linear interpolation of the nonzero T^* points gives an extrapolated U_{ext} value, defined as $T^*(U_{\text{ext}}) \to 0$, that is close to the critical value U^* associated with the Mott transition obtained from the specific heat curves. While it is not clear why or even whether the relationship $T^*(U) \sim (U - U^*)$ holds, this simple analysis lends further support to the conclusion that the interaction impacts different sites in distinct ways inside the Mott phase.

To further validate our findings of site-selective correlations, we perform an analytical continuation of $G_z(\tau)$ [69] to extract the z-resolved spectral functions $A_z(\omega)$. Figures 4(a)–4(d) show their temperature dependence for $U = 7$. At high temperatures, $A_z(\omega)$ has the typical metallic shape, with $A_3(\omega = 0)$ being the largest. However, as temperature is lowered and a gap starts to form, the site-selective character of the transition emerges. First, the separation between the finite-ω peaks is larger for $A_3(\omega)$. Second, as the temperature is lowered even further, a Kondo-resonance peak at $\omega = 0$ can be seen in $A_7(\omega)$. Interestingly, such a peak often emerges in single-site DMFT simulations of the Hubbard model [70,71]. Since DMFT is exact in the limit $z \to \infty$, it is reasonable that mean-field features in $A_z(\omega)$ emerge for larger z.

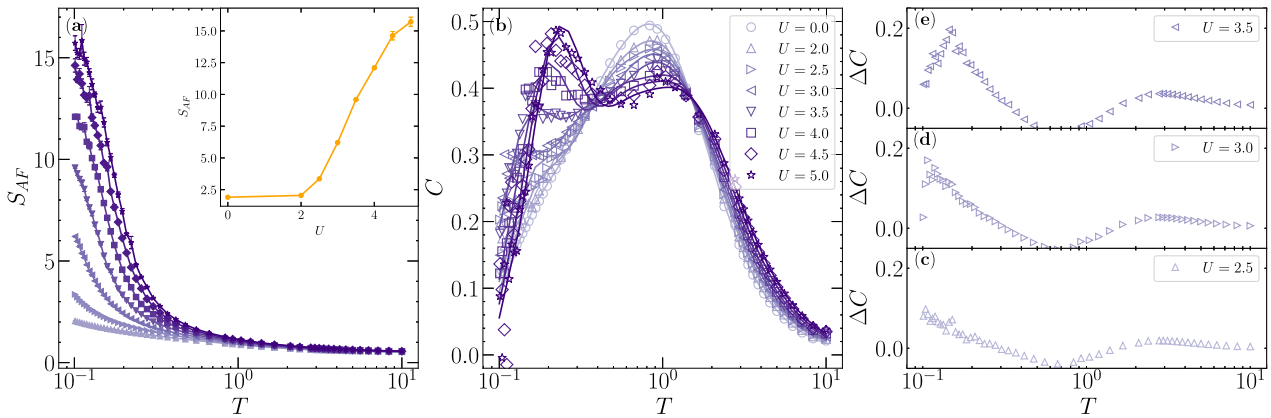

FIG. 5. Antiferromagnetic phase transition on the kite-and-dart tiling. (a) AF structure factor S_{AF}; (b) specific heat C, both as a function of temperature T on a logarithmic scale. Increasing interaction strength U is distinguished by the color scale from light-purple to dark-purple. S_{AF} behavior at low temperature $T = 0.1$ is highlighted in (a) inset. (c)–(e) show ΔC, defined as $C(U) - C(U = 0)$, for three U values: $U = 2.5$, 3.0, and 3.5 (from bottom to top).

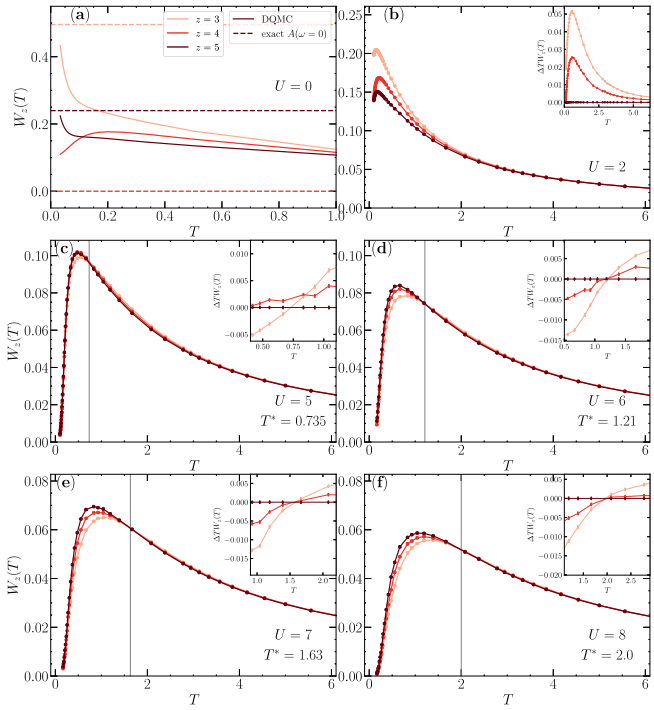

FIG. 6. The z-projected zero-energy spectral function proxy $W_z(T)$ [see Eq. (2) for definition] with increasing interaction strength, in the case of the kite-and-dart tiling. The insets in (b)–(f) show $\Delta TW_z(T) \equiv TW_z(T) - TW_5(T)$, highlighting the crossing points marked by the vertical line in the main panels.

To perform a more quantitative analysis, Figs. 4(e) and 4(f) show the T dependence of the spectral function evaluated at zero energy, $A_z(\omega = 0)$, for $U = 4$ and 8, respectively. For $U = 4$, the hierarchy observed from the curves is that $A_3(0)$ is the largest for all temperatures. Conversely, for $U = 8$, the hierarchy is reversed at low temperatures, with $A_3(0)$ generally assuming the smallest value. Moreover, a full gap is observed at low enough temperatures.

B. Kite-and-dart tiling

Similar results were also obtained for the kite-and-dart tiling. Figure 5 shows the antiferromagnetic structure factor S_{AF} and specific heat $C(T)$ as a function of temperature for various interaction strength values. Similarly to the rhombus case, AF order develops when temperature is lowered for sufficiently strong coupling strength. The behavior of specific heat $C(T)$ shows the same trend as the rhombus case: for small interaction values, a broad one-peak shape signals a nonordered phase, whereas for $U \geqslant 3.0$, a two-peak structure signals the onset of the ordered magnetic state. Thus we estimate $U_c = 3.0$, slightly smaller than the value obtained for the rhombus tilinge.

Like in the rhombus case, a site-selective behavior for the correlation effects is seen on the kite-and-dart tiling. Figure 6 shows the proxy of the z-projected zero-energy spectral function $W_z(T)$ for the kite-and-dart case. In the weak coupling case $U = 2$, displayed in panel (b), the sites with the smallest coordination number $z = 3$ have the largest spectral function

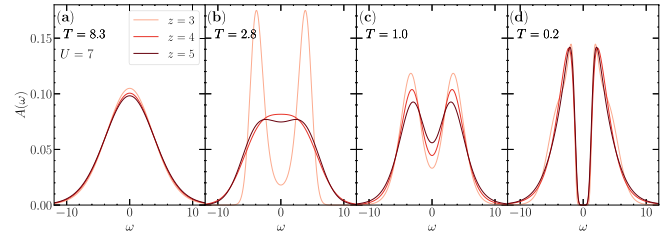

FIG. 7. The z-projected spectral function $A_z(\omega)$ obtained via analytical continuation for $U = 7$ and at various temperature values T, in the case of the kite-and-dart tiling.

proxy; these are also the sites that contribute the most to the zero-energy peak of the noninteracting density of states. In the strong coupling case $U \geqslant 5.0$, however, a reversal occurs and the sites with $z = 3$ display the smallest spectral function proxy below a characteristic temperature T^* where the $W_z(T)$ curves for different z values cross.

Finally, we perform an analytical continuation to obtain the z-resolved spectral function $A_z(w)$ for the kite-and-dart geometry. Figure 7 shows $A_z(w)$ at strong coupling $U = 7$ as temperature is lowered; On the one hand, a gap opens at the lowest temperature $T = 0.208$, corresponding to the Mott phase as discussed in the previous section. On the other hand, comparing panels (a) and (c), we see the reversal in the hierarchy of $A_z(\omega = 0)$ values: at higher temperatures, $A_3(0) > A_4(0) > A_5(0)$, whereas at low temperatures, $A_5(0) > A_4(0) > A_3(0)$. A systematic analysis of the temperature and interaction-strength dependence of $A_z(0)$ is shown in Fig. 8. For $U = 2$, $A_3(0)$ is generally the largest whereas for $U = 8$, $A_5(0)$ is generally the largest. It is interesting to note that for intermediate values of U, e.g. $U = 4$, there are regimes where $A_4(0)$ is the largest. This could be a consequence of the fact that in the kite-and-dart tiling, the $z = 5$ sites also contribute to the zero-energy peak in the global DOS, although the dominant contribution still comes from the $z = 3$ sites. We note that, for strong interactions $U \geqslant 6.0$, a gap opening can be seen approaching low temperatures, signaling the Mott transition.

IV. DISCUSSION AND SUMMARY

Our result of site-selective correlations in interacting quasicrystals qualitatively agrees with a RDMFT investigation of the doped Hubbard model on the rhombus tiling

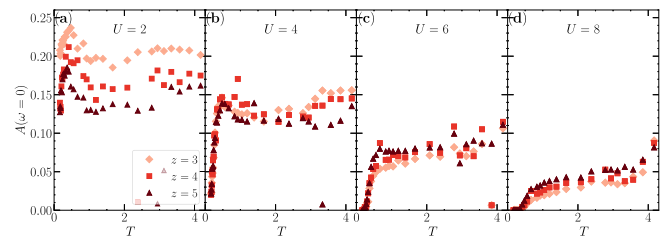

FIG. 8. The z-projected spectral function $A_z(\omega)$ obtained via analytical continuation for various fixed interaction strength values U, as a function of temperature T, in the kite-and-dart tiling.

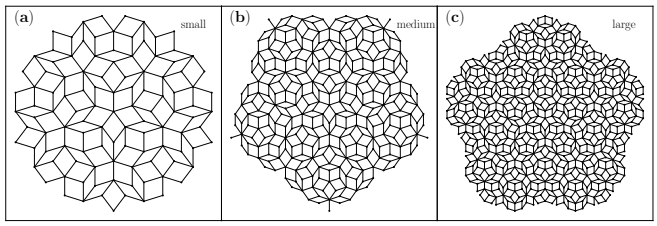

FIG. 9. The "small" (a), "medium" (b), and "large" (c) versions of the Penrose rhombus tiling sampled in this study. Results on medium tiling are shown in Sec. III A; results on small and large tilings are presented here.

[30], which found that added carriers dope more the sites with smaller (larger) z at weak (strong) coupling. Our finding is also reminiscent of the site-selective behavior observed in a recent CPA study of the Hubbard model on commensurately-twisted tetragonal bilayers [72]. More broadly, the concept that correlations affect different sites in distinct ways generalizes the notion of orbital-selective correlations, by which different orbitals experience the effects of correlations differently [73,74]. In analogy to the scenario of an orbital-selective Mott transition, it is an interesting question whether a site-selective Mott transition could emerge in quasicrystals.

In summary, our DQMC simulations demonstrate that, in interacting quasicrystals, the onsite repulsion affects sites with different coordination numbers in distinct ways. Specifically, the LDOS is more strongly suppressed on sites with the smallest z, which for the two types of Penrose quasicrystals studied here correspond to $z = 3$. Interestingly, in a mean-field approach to the Hubbard model on a periodic lattice, the critical U^* signaling the Mott transition scales as $U^* \sim 1/z$, since the bandwidth scales as z [75]. It is intriguing that in a quasicrystal, where z is defined locally and there is no bandwidth, the sites with smallest z are more strongly affected by interactions. More importantly, in the Penrose tilings investigated here, the $z = 3$ sites are the ones that contribute the most to the zero-energy peak in the global DOS, which play the same role as a flat band in periodic lattices. Thus our results reveal a subtle interplay between flat-band physics and interactions, pointing to the importance of the real-space structure of flat bands. Indeed, while featureless in momentum space, flat-bands often display nontrivial patterns in real space. This is not exclusive to quasicrystals: in the kagome lattice, the flat band has a nontrivial projection onto the sublattices [76].

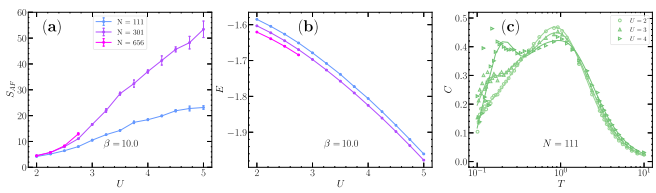

FIG. 10. Energy and antiferromagnetic structure factor S_{AF} for three different sizes of the Penrose rhombus tiling. Here, N refers to the total number of sites.

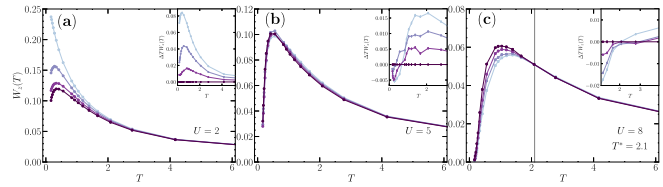

FIG. 11. LDOS proxy for $U = 2$, 5 and 8, akin to Fig. 3, but here for the small Penrose rhombus tiling.

Similarly, in twisted bilayer graphene, the flat band emerges primarily from the AA stacking sites [77]. It will be interesting to investigate whether site selectivity also emerges in these flat-band settings.

ACKNOWLEDGMENTS

We thank J. Schmalian for useful discussions. Y.Z. and R.M.F were supported by the Air Force Office of Scientific Research under Award No. FA9550-21-1-0423. R.T.S. was supported by the Grant No. DE-SC0014671 funded by the U.S. Department of Energy, Office of Science.

APPENDIX A: DETAILS OF THE DETERMINANTAL QUANTUM MONTE CARLO APPROACH

We employed the standard determinantal quantum Monte Carlo (DQMC) method in this work [78]. After discretizing the inverse temperature β in the imaginary time axis $\beta = L_\tau \Delta\tau$, one can decouple the kinetic energy K and the interaction V of the Hamiltonian, since the penalty can be minimized by setting $\Delta\tau \to 0$. After decoupling, the Hubbard interaction term can be dealt with via the (discrete) Hubbard-Stratonovich (HS) transformation

$$e^{-U\Delta\tau\left(n_{\mathbf{i}\uparrow}-\frac{1}{2}\right)\left(n_{\mathbf{i}\downarrow}-\frac{1}{2}\right)} = \frac{1}{2}e^{-\frac{U\Delta\tau}{4}}\sum_{S_{\mathbf{i}}} e^{\lambda S_{\mathbf{i}}\left(n_{\mathbf{i}\uparrow}-n_{\mathbf{i}\downarrow}\right)}, \qquad \text{(A1)}$$

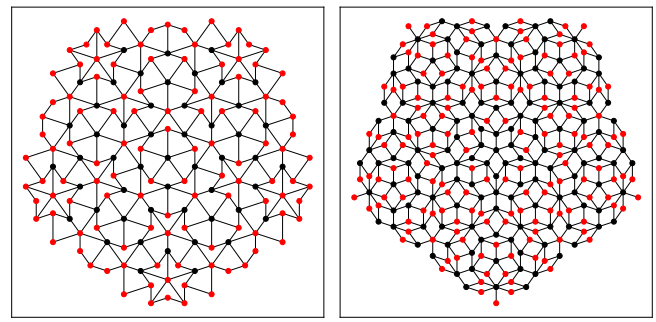

FIG. 12. Real-space structure of the zero-energy peak for the lattice studied in this work, namely kite-and-dart tiling (left) and the rhombus tiling (right).

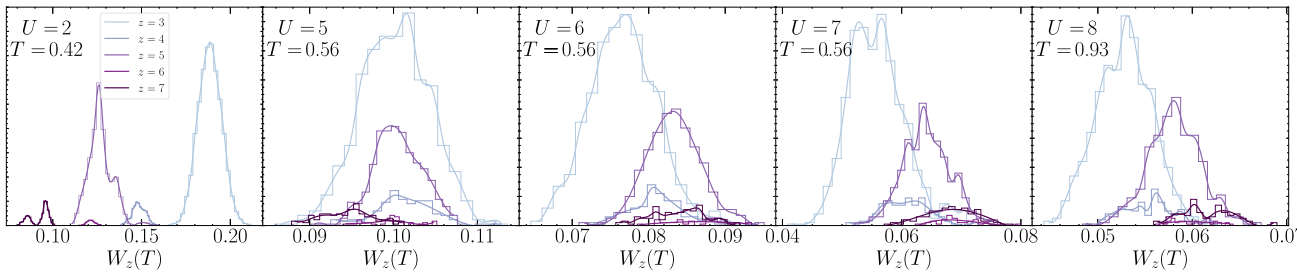

FIG. 13. Spread of local density of states (LDOS) data for $U = 2,\ 5,\ 6,\ 7$, and 8, taken at the temperature T where $W_z(T)$ is maximized for each U.

where $\cosh\lambda = e^{\frac{U\Delta\tau}{2}}$, and the additional HS field $S_{\mathbf{i}} = \pm 1$ is an Ising-like variable. The partition function can be written as

$$\begin{aligned} Z &= \sum \mathrm{Tr}\, e^{-\beta\hat{H}} = \sum \mathrm{Tr} \prod e^{-\Delta\tau\hat{H}} \\ &= \sum \mathrm{Tr} \prod e^{-\Delta\tau\hat{K}} e^{-\Delta\tau\hat{V}} \\ &= \sum \det\left[\mathbf{I} + \prod e^{-\Delta\tau\mathbf{K}} e^{-\Delta\tau\mathbf{V}(S_{\mathbf{i},l})}\right] \qquad \text{(A2)} \\ &= \sum \det \mathbf{M}, \qquad \text{(A3)} \end{aligned}$$

where the sum is over the HS field $\{S_{\mathbf{i},l}\}$ and the trace is over the fermion operator.

Measurements are carried out via Green's functions and Wick's construction

$$G_\sigma(i,j) = \langle \hat{c}_{\mathbf{i}\sigma} \hat{c}^\dagger_{\mathbf{j}\sigma} \rangle = [\mathbf{M}_\sigma]^{-1}_{ij}. \qquad \text{(A4)}$$

For example, the anti-ferromagnetic (AF) structure factor is defined as [79]

$$S_{AF} = \sum_{\mathbf{r}} (-1)^{\mathbf{r}} m(\mathbf{r}), \qquad \text{(A5)}$$

where the spin-spin correlation functions are defined as

$$m(\mathbf{r}) = \tfrac{1}{3}[2m^{xx}(\mathbf{r}) + m^{zz}(\mathbf{r})] \qquad \text{(A6)}$$

and

$$\begin{aligned} m^{xx}(\mathbf{r}) &= \langle S^-(\mathbf{i}+\mathbf{r}) S^+(\mathbf{i}) \rangle, \\ m^{zz}(\mathbf{r}) &= \langle S^z(\mathbf{i}+\mathbf{r}) S^z(\mathbf{i}) \rangle, \qquad \text{(A7)} \end{aligned}$$

where

$$\begin{aligned} S^+(\mathbf{i}) &= c_{\mathbf{i}\downarrow} c^\dagger_{\mathbf{i}\uparrow}, \quad S^-(\mathbf{i}) = c_{\mathbf{i}\uparrow} c^\dagger_{\mathbf{i}\downarrow}, \\ S^z(\mathbf{i}) &= \tfrac{1}{2}(n_{\mathbf{i}\uparrow} - n_{\mathbf{i}\downarrow}) \qquad \text{(A8)} \end{aligned}$$

can be directly accessed via Green's function.

To ensure reliable statistical results, we used $\Delta\tau = 0.1$, as well as Monte Carlo steps of $N_{\text{warms}} = 5\,000$–$10\,000$ for thermalization sweeps and $N_{\text{meas}} = 80\,000$ for measurement sweeps.

APPENDIX B: FINITE SIZE ANALYSIS

We presented in Section III the results of Penrose rhombus tiling of size $N = 301$; additional simulations were performed on a smaller tilings with $N = 111$ [denoted as "small," shown in Fig. 9(a)] and a larger tiling with $N = 656$ [denoted as "large," shown in Fig. 9(c)] to eliminate possible finite size effect. All three tilings include a symmetry center and retain fivefold symmetry.

Similar to the medium-size tiling discussed in Sec. III, both small and large tilings display the same global physical features, such as energy E and AF structure factor S_{AF}, as shown in Figs. 10(a) and 10(b). Specific heat analysis on the small tiling is shown in Fig. 10(c), where the one-peak to two-peaks transition can be seen at $U \sim 3.0$, in reasonable agreement with the result shown in Fig. 2.

Local quantities such as the LDOS are examined as well. Shown in Fig. 11 is the LDOS proxy $W_z(T)$, defined in Eq. (2), on the small Penrose rhombus tiling, akin to Fig. 3. The exact same "site-selective" behavior is observed here on the small tiling, namely: at $U = 2$, $W_3(T)$ remains the largest throughout the temperature range sampled, whereas for $U = 8$, the order is reversed and sites with larger coordination number z contribute the most for $A_z(\omega = 0)$ at low temperatures.

APPENDIX C: REAL SPACE STRUCTURE OF THE "FLAT-BAND"

The real space structure of the "flat-band" on the Penrose kite-and-dart and rhombus tiling is nontrivial [16]. We reproduce their findings here by plotting the projection of the wave-function of the zero-energy states on the Penrose tiling sites in Fig. 12. The red sites are those that have a finite overlap with the zero-energy states. These sites are not localized, in contrast to some periodic lattices that have a flat band, e.g., the kagome lattice. Most of these sites have coordination number $z = 3$, as shown and discussed in Fig. 1.

APPENDIX D: SPREAD OF THE LDOS PROXY $W_z(T)$

We presented and analyzed the proxy for the local density of states (LDOS) $W_z(T)$ in Sec. III, which was obtained by averaging over sites with the same coordination number z. Here we further support our analysis by plotting the variance of the $W_z(T)$ data in Fig. 13. We choose the temperature at which $W_z(T)$ is maximized for each interaction strength. Sites with the smallest coordination number $z = 3$ have the largest W_z for weak interactions and the smallest W_z for strong interactions. At weak coupling $U = 2$, the spread of the LDOS proxy for the $z = 3$ sites forms a sharp peak, separating from the sites with other z values. As U increases, the peak for $z = 3$ shifts steadily to the left.

[1] N. Regnault, Y. Xu, M.-R. Li, D.-S. Ma, M. Jovanovic, A. Yazdani, S. S. Parkin, C. Felser, L. M. Schoop, N. P. Ong *et al.*, Catalogue of flat-band stoichiometric materials, Nature (London) **603**, 824 (2022).

[2] P. M. Neves, J. P. Wakefield, S. Fang, H. Nguyen, L. Ye, and J. G. Checkelsky, Crystal net catalog of model flat band materials, npj Comput. Mater. **10**, 39 (2024).

[3] Y. Cao, V. Fatemi, A. Demir, S. Fang, S. L. Tomarken, J. Y. Luo, J. D. Sanchez-Yamagishi, K. Watanabe, T. Taniguchi, E. Kaxiras *et al.*, Correlated insulator behaviour at half-filling in magic-angle graphene superlattices, Nature (London) **556**, 80 (2018).

[4] Y. Cao, V. Fatemi, S. Fang, K. Watanabe, T. Taniguchi, E. Kaxiras, and P. Jarillo-Herrero, Unconventional superconductivity in magic-angle graphene superlattices, Nature (London) **556**, 43 (2018).

[5] R. Bistritzer and A. H. MacDonald, Moiré bands in twisted double-layer graphene, Proc. Natl. Acad. Sci. USA **108**, 12233 (2011).

[6] W. R. Meier, M.-H. Du, S. Okamoto, N. Mohanta, A. F. May, M. A. McGuire, C. A. Bridges, G. D. Samolyuk, and B. C. Sales, Flat bands in the CoSn-type compounds, Phys. Rev. B **102**, 075148 (2020).

[7] M. Kang, S. Fang, L. Ye, H. C. Po, J. Denlinger, C. Jozwiak, A. Bostwick, E. Rotenberg, E. Kaxiras, J. G. Checkelsky *et al.*, Topological flat bands in frustrated kagome lattice CoSn, Nat. Commun. **11**, 4004 (2020).

[8] M. Kang, L. Ye, S. Fang, J.-S. You, A. Levitan, M. Han, J. I. Facio, C. Jozwiak, A. Bostwick, E. Rotenberg *et al.*, Dirac fermions and flat bands in the ideal kagome metal FeSn, Nat. Mater. **19**, 163 (2020).

[9] L. Ye, S. Fang, M. Kang, J. Kaufmann, Y. Lee, C. John, P. M. Neves, S. F. Zhao, J. Denlinger, C. Jozwiak *et al.*, Hopping frustration-induced flat band and strange metallicity in a kagome metal, Nat. Phys. **20**, 610 (2024).

[10] J. Huang, L. Chen, Y. Huang, C. Setty, B. Gao, Y. Shi, Z. Liu, Y. Zhang, T. Yilmaz, E. Vescovo *et al.*, Non-Fermi liquid behaviour in a correlated flat-band pyrochlore lattice, Nat. Phys. **20**, 603 (2024).

[11] D. Shechtman, I. Blech, D. Gratias, and J. W. Cahn, Metallic phase with long-range orientational order and no translational symmetry, Phys. Rev. Lett. **53**, 1951 (1984).

[12] D. Levine and P. J. Steinhardt, Quasicrystals: A new class of ordered structures, Phys. Rev. Lett. **53**, 2477 (1984).

[13] M. Kohmoto and B. Sutherland, Electronic states on a Penrose lattice, Phys. Rev. Lett. **56**, 2740 (1986).

[14] M. Arai, T. Tokihiro, T. Fujiwara, and M. Kohmoto, Strictly localized states on a two-dimensional Penrose lattice, Phys. Rev. B **38**, 1621 (1988).

[15] T. Rieth and M. Schreiber, Identification of spatially confined states in two-dimensional quasiperiodic lattices, Phys. Rev. B **51**, 15827 (1995).

[16] E. Day-Roberts, R. M. Fernandes, and A. Kamenev, Nature of protected zero-energy states in Penrose quasicrystals, Phys. Rev. B **102**, 064210 (2020).

[17] E. C. Andrade, A. Jagannathan, E. Miranda, M. Vojta, and V. Dobrosavljević, Non-Fermi-liquid behavior in metallic quasicrystals with local magnetic moments, Phys. Rev. Lett. **115**, 036403 (2015).

[18] N. Takemori and A. Koga, Local electron correlations in a two-dimensional Hubbard model on the Penrose lattice, J. Phys. Soc. Jpn. **84**, 023701 (2015).

[19] S. Thiem and J. T. Chalker, Magnetism in rare-earth quasicrystals: RKKY interactions and ordering, Europhys. Lett. **110**, 17002 (2015).

[20] S. Sakai, N. Takemori, A. Koga, and R. Arita, Superconductivity on a quasiperiodic lattice: Extended-to-localized crossover of Cooper pairs, Phys. Rev. B **95**, 024509 (2017).

[21] A. Koga and H. Tsunetsugu, Antiferromagnetic order in the Hubbard model on the Penrose lattice, Phys. Rev. B **96**, 214402 (2017).

[22] R. N. Araújo and E. C. Andrade, Conventional superconductivity in quasicrystals, Phys. Rev. B **100**, 014510 (2019).

[23] F. Flicker, S. H. Simon, and S. A. Parameswaran, Classical dimers on Penrose tilings, Phys. Rev. X **10**, 011005 (2020).

[24] R. Ghadimi, T. Sugimoto, and T. Tohyama, Mean-field study of the Bose-Hubbard model in the Penrose lattice, Phys. Rev. B **102**, 224201 (2020).

[25] Y. Cao, Y. Zhang, Y.-B. Liu, C.-C. Liu, W.-Q. Chen, and F. Yang, Kohn-Luttinger mechanism driven exotic topological superconductivity on the Penrose lattice, Phys. Rev. Lett. **125**, 017002 (2020).

[26] N. Takemori, R. Arita, and S. Sakai, Physical properties of weak-coupling quasiperiodic superconductors, Phys. Rev. B **102**, 115108 (2020).

[27] R. Gautier, H. Yao, and L. Sanchez-Palencia, Strongly interacting Bosons in a two-dimensional quasicrystal lattice, Phys. Rev. Lett. **126**, 110401 (2021).

[28] J. B. Profe, C. Honerkamp, S. Achilles, and D. M. Kennes, Electronic instabilities in Penrose quasicrystals: Competition, coexistence, and collaboration of order, Phys. Rev. Res. **3**, 023180 (2021).

[29] S. Sakai, R. Arita, and T. Ohtsuki, Hyperuniform electron distributions controlled by electron interactions in quasicrystals, Phys. Rev. B **105**, 054202 (2022).

[30] S. Sakai and N. Takemori, Doped Mott insulator on a Penrose tiling, Phys. Rev. B **105**, 205138 (2022).

[31] E. Gottlob and U. Schneider, Hubbard models for quasicrystalline potentials, Phys. Rev. B **107**, 144202 (2023).

[32] M. A. Keskiner, O. Erten, and M. Ö. Oktel, Kitaev-type spin liquid on a quasicrystal, Phys. Rev. B **108**, 104208 (2023).

[33] Y.-B. Liu, Y. Zhang, W.-Q. Chen, and F. Yang, High-angular-momentum topological superconductivities in twisted bilayer quasicrystal systems, Phys. Rev. B **107**, 014501 (2023).

[34] Y.-B. Liu, J. Zhou, and F. Yang, Nematic superconductivity and its critical vestigial phases in the quasicrystal, Phys. Rev. Lett. **133**, 136002 (2024).

[35] V. Gali, M. Hecker, and R. M. Fernandes, Critical nematic phase with pseudogaplike behavior in twisted bilayers, Phys. Rev. Lett. **133**, 236501 (2024).

[36] M. Hecker, A. Rastogi, D. F. Agterberg, and R. M. Fernandes, Classification of electronic nematicity in three-dimensional crystals and quasicrystals, Phys. Rev. B **109**, 235148 (2024).

[37] L. Liu, Z.-X. Li, and F. Yang, Superconductivity and charge density wave in the holstein model on the penrose lattice, Phys. Rev. Lett. **134**, 206001 (2025).

[38] C. W. Duncan, S. Manna, and A. E. B. Nielsen, Topological models in rotationally symmetric quasicrystals, Phys. Rev. B **101**, 115413 (2020).

[39] S. Manna, S. K. Das, and B. Roy, Noncrystalline topological superconductors, Phys. Rev. B **109**, 174512 (2024).

[40] K. Kamiya, T. Takeuchi, N. Kabeya, N. Wada, T. Ishimasa, A. Ochiai, K. Deguchi, K. Imura, and N. Sato, Discovery of superconductivity in quasicrystal, Nat. Commun. **9**, 154 (2018).

[41] A. Uri, S. C. de la Barrera, M. T. Randeria, D. Rodan-Legrain, T. Devakul, P. J. Crowley, N. Paul, K. Watanabe, T. Taniguchi, R. Lifshitz *et al.*, Superconductivity and strong interactions in a tunable moiré quasicrystal, Nature (London) **620**, 762 (2023).

[42] Y. Tokumoto, K. Hamano, S. Nakagawa, Y. Kamimura, S. Suzuki, R. Tamura, and K. Edagawa, Superconductivity in a van der Waals layered quasicrystal, Nat. Commun. **15**, 1529 (2024).

[43] R. Tamura, Y. Muro, T. Hiroto, K. Nishimoto, and T. Takabatake, Long-range magnetic order in the quasicrystalline approximant Cd_6Tb, Phys. Rev. B **82**, 220201(R) (2010).

[44] A. Ishikawa, T. Fujii, T. Takeuchi, T. Yamada, Y. Matsushita, and R. Tamura, Antiferromagnetic order is possible in ternary quasicrystal approximants, Phys. Rev. B **98**, 220403(R) (2018).

[45] P. Das, A. Kreyssig, G. S. Tucker, A. Podlesnyak, F. Ye, M. Matsuda, T. Kong, S. L. Bud'ko, P. C. Canfield, R. Flint, P. P. Orth, T. Yamada, R. J. McQueeney, and A. I. Goldman, Short-range magnetic correlations in quasicrystalline *i*-Tb-Cd, Phys. Rev. B **108**, 134421 (2023).

[46] K. Deguchi, S. Matsukawa, N. K. Sato, T. Hattori, K. Ishida, H. Takakura, and T. Ishimasa, Quantum critical state in a magnetic quasicrystal, Nat. Mater. **11**, 1013 (2012).

[47] S. Matsukawa, K. Deguchi, K. Imura, T. Ishimasa, and N. K. Sato, Pressure-driven quantum criticality and T/H scaling in the icosahedral Au–Al–Yb approximant, J. Phys. Soc. Jpn. **85**, 063706 (2016).

[48] A. Khansili, Y.-C. Huang, U. Häussermann, C. P. Gomez, and A. Rydh, Precursor to quantum criticality in Ce-Au-Al quasicrystal approximants, Phys. Rev. Res. **7**, 013277 (2025).

[49] A. Jagannathan and M. Duneau, An eightfold optical quasicrystal with cold atoms, Europhys. Lett. **104**, 66003 (2013).

[50] T. A. Corcovilos and J. Mittal, Two-dimensional optical quasicrystal potentials for ultracold atom experiments, Appl. Opt. **58**, 2256 (2019).

[51] J.-C. Yu, S. Bhave, L. Reeve, B. Song, and U. Schneider, Observing the two-dimensional Bose glass in an optical quasicrystal, Nature (London) **633**, 338 (2024).

[52] M. Kohmoto, B. Sutherland, and K. Iguchi, Localization of optics: Quasiperiodic media, Phys. Rev. Lett. **58**, 2436 (1987).

[53] Z. V. Vardeny, A. Nahata, and A. Agrawal, Optics of photonic quasicrystals, Nat. Photonics **7**, 177 (2013).

[54] Z. Liu, Q. Gao, Y. Li, X. Liu, F. Zhang, D. S. Kim, Y. Ni, M. Mackenzie, H. Abudayyeh, K. Watanabe *et al.*, Field-tunable valley coupling and localization in a dodecagonal semiconductor quasicrystal, arXiv:2408.02176.

[55] L. C. Collins, T. G. Witte, R. Silverman, D. B. Green, and K. K. Gomes, Imaging quasiperiodic electronic states in a synthetic Penrose tiling, Nat. Commun. **8**, 15961 (2017).

[56] R. Blankenbecler, D. J. Scalapino, and R. L. Sugar, Monte Carlo calculations of coupled Boson-Fermion systems. I, Phys. Rev. D **24**, 2278 (1981).

[57] R. T. Scalettar, D. J. Scalapino, and R. L. Sugar, New algorithm for the numerical simulation of fermions, Phys. Rev. B **34**, 7911 (1986).

[58] S. R. White, R. L. Sugar, and R. T. Scalettar, Algorithm for the simulation of many-electron systems at low temperatures, Phys. Rev. B **38**, 11665 (1988).

[59] T. Paiva, R. T. Scalettar, W. Zheng, R. R. P. Singh, and J. Oitmaa, Ground-state and finite-temperature signatures of quantum phase transitions in the half-filled Hubbard model on a honeycomb lattice, Phys. Rev. B **72**, 085123 (2005).

[60] C. N. Varney, C.-R. Lee, Z. J. Bai, S. Chiesa, M. Jarrell, and R. T. Scalettar, Quantum Monte Carlo study of the two-dimensional fermion Hubbard model, Phys. Rev. B **80**, 075116 (2009).

[61] D. P. Arovas, E. Berg, S. A. Kivelson, and S. Raghu, The Hubbard model, Annu. Rev. Condens. Matter Phys. **13**, 239 (2022).

[62] M. Qin, T. Schäfer, S. Andergassen, P. Corboz, and E. Gull, The Hubbard model: A computational perspective, Annu. Rev. Condens. Matter Phys. **13**, 275 (2022).

[63] A. Georges and W. Krauth, Physical properties of the half-filled Hubbard model in infinite dimensions, Phys. Rev. B **48**, 7167 (1993).

[64] D. Vollhardt, Characteristic crossing points in specific heat curves of correlated systems, Phys. Rev. Lett. **78**, 1307 (1997).

[65] N. Chandra, M. Kollar, and D. Vollhardt, Nearly universal crossing point of the specific heat curves of Hubbard models, Phys. Rev. B **59**, 10541 (1999).

[66] N. Trivedi and M. Randeria, Deviations from Fermi-liquid behavior above Tc in 2D short coherence length superconductors, Phys. Rev. Lett. **75**, 312 (1995).

[67] C. B. Mendl, E. A. Nowadnick, E. W. Huang, S. Johnston, B. Moritz, and T. P. Devereaux, Doping dependence of ordered phases and emergent quasiparticles in the doped Hubbard-Holstein model, Phys. Rev. B **96**, 205141 (2017).

[68] W. O. Wang, J. K. Ding, B. Moritz, E. W. Huang, and T. P. Devereaux, DC Hall coefficient of the strongly correlated Hubbard model, npj Quantum Mater. **5**, 1 (2020).

[69] J. Kaufmann and K. Held, ana_cont: Python package for analytic continuation, Comput. Phys. Commun. **282**, 108519 (2023).

[70] T. Pruschke, D. L. Cox, and M. Jarrell, Hubbard model at infinite dimensions: Thermodynamic and transport properties, Phys. Rev. B **47**, 3553 (1993).

[71] G. Kotliar, E. Lange, and M. J. Rozenberg, Landau theory of the finite temperature Mott transition, Phys. Rev. Lett. **84**, 5180 (2000).

[72] X.-C. Jiang, Z. Ruan, and Y.-Z. Zhang, Site-selective insulating phase in a twisted bilayer Hubbard model, Phys. Rev. B **109**, 085104 (2024).

[73] L. de'Medici, A. Georges, and S. Biermann, Orbital-selective Mott transition in multiband systems: Slave-spin representation and dynamical mean-field theory, Phys. Rev. B **72**, 205124 (2005).

[74] M. Vojta, Orbital-selective Mott transitions: Heavy fermions and beyond, J. Low Temp. Phys. **161**, 203 (2010).

[75] C. K. Thomas, T. H. Barter, T.-H. Leung, M. Okano, G.-B. Jo, J. Guzman, I. Kimchi, A. Vishwanath, and D. M. Stamper-Kurn, Mean-field scaling of the superfluid to Mott insulator transition in a 2D optical superlattice, Phys. Rev. Lett. **119**, 100402 (2017).

[76] K. Zeng and Z. Wang, Interorbital antisymmetric hopping generated flat bands on kagome and pyrochlore lattices, npj Quantum Mater. **9**, 74 (2024).

[77] Z.-D. Song and B. A. Bernevig, Magic-angle twisted bilayer graphene as a topological heavy fermion problem, Phys. Rev. Lett. **129**, 047601 (2022).

[78] J. E. Hirsch, D. J. Scalapino, R. L. Sugar, and R. Blankenbecler, Efficient Monte Carlo procedure for systems with fermions, Phys. Rev. Lett. **47**, 1628 (1981).

[79] E. Khatami, R. R. P. Singh, W. E. Pickett, and R. T. Scalettar, Magnetic correlations and pairing in the 1/5-depleted square lattice Hubbard model, Phys. Rev. Lett. **113**, 106402 (2014).